Multi-scale in-situ micro-mechanical characterization of Polymer Core Solder Ball (PCSB) coatings for BGA interconnections

Irati Malkorra, Sergio Sao Joao, U. Costa, D. Chalavoux, S. Bucher, N. Perardel, Guillaume Kermouche

Multi-scale in-situ micro-mechanical characterisation of Polymer Core Solder Ball (PCSB) coatings for BGA interconnections

March 7, 2024

I. Malkorra [1], S. Sao-Joao [1], U. Costa [2], D. Chalavoux [2], S. Bucher [3], N. Perardel [4], G. Kermouche [1]

[1] Mines Saint-Etienne, Univ Lyon, CNRS, UMR 5307 LGF, F - 42023 Saint-Etienne, France

[2] THALES Avionics SAS, 25, rue Jules Védrines, F-26000, Valence, France

[3] LIFCO Industrie, HEF Group, 7 Rue Salvador Dali, 42000 Saint-Étienne, France

[4] Nicomatic SA, 173 Rue des Fougères, 74890 Bons-en-Chablais, France

Highlights

- Bulk material properties are commonly used to describe electroless plated coatings on the field of electronics.
- For the first time, the material properties of the coatings of a PCSB (Polymer Core Solder Balls) solder ball for BGA interconnections are characterized by micromechanical tests.
- Electroless plated copper and nickel coatings present a higher yielding limit and a lower young's modulus than the corresponding bulk materials.
- The microstructures of copper and nickel coatings are nanostructured and amorphous.
- The use of bulk material properties is not correct when describing electroless plated coatings.

Keywords: PCSB, electroless copper, electroless nickel, microstructure, in-situ micropillar compression, FEM

Abstract

In the field of electronic packaging, the manufacturing processes involve electroless plating. The microstructure of these materials differs from bulk materials, so do their mechanical properties. However, bulk material properties are commonly attributed to them. This paper is focused on the characterisation of the mechanical properties of a multilayer coating of copper and nickel-phosphorus deposited on a Polymer Core Solder Ball (PCSB) used for BGA (Ball Grid Array) connections. In this coating, the copper is nanocrystalline, while the nickel-phosphorus is amorphous. In order to understand the influence of these microstructural differences on the mechanical properties of the PCSB, a multiscale study is performed. First, at the microscopical scale, the characterisation of the mechanical properties (Young modulus (E) and Yielding strength (σ)) of two coatings (Cu, Ni-P) is conducted. For this purpose, insitu micro-mechanical tests (Micro pillar compression and nanoindentation) are carried out. Then, at the mesoscopical scale, the previous properties are validated by applying a compressive loading to a PCSB solder ball. A correlation between the numerical and experimental approaches is performed and revealed that the coating properties are different from those of the bulk material.

1 Introduction

The increasing need for smaller electronic components has driven the semiconductor industry to develop extremely compact systems such as High Density Interconnects (HDI) Printed Circuit Boards (PCB) and System In Package (SIP) modules. These technologies use high performance interconnection systems such as Ball Grid Arrays (BGA) [1,2] to connect the chip carrier or the SIP module to the PCB. Solder balls are responsible to ensure both the stand-off and the electrical connection of the printed circuit board assembly (PCBA). Solder balls are the most popular,however, solder columns or Polymer Core Solder Balls (PCSB) can also be used [3]. Figure 1-a shows a schema of a PCBA with a BGA type surface mounted device (SMD) on the printed circuit board.

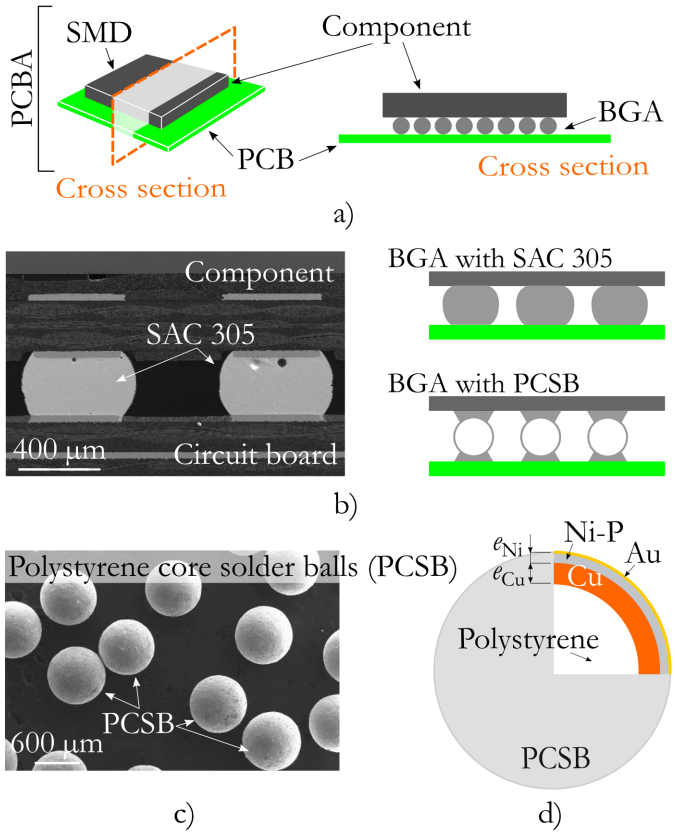

Figure 1: a) Illustration of the Surface Mounted Device (SMD) with a BGA connection in a printed circuit board (PCB), b) Scanning Electron Microscope (SEM) image showing the details of the BGA with SAC305 and illustration of a PCSB mounted with the solder paste to the component and the PCB, c) polystyrene core solder balls (PCSB) of 750 µm in diameter, d) an schematic figure of the structure of a PCSB.

Since electronic systems are used in high-end applications like in automotive and aerospace safety systems, their reliability has become a major issue for both industry and research fields. As reported in [4], temperature variations are the main factor in electronic components failure (in 55% of the cases). Thermal cycling induces thermal fatigue in assemblies, particularly in solder joints, due to the different coefficients of thermal expansion (CTE) between each material. Therefore, it is essential that the solders are mechanically, physically and chemically optimised to provide durable interconnection struc-

tures.

To date, most of the solder balls used in BGA are made of a lead-tin alloy (Pb 90%-Sn 10%). Their chemical, thermal and mechanical properties provide reliable solders [5,6]. However, the European Union Directives 2012/19/EU on Waste Electrical and Electronical Equipment (WEEE) and 2011/65/EU on the Restriction of the use of certain Hazardous Substances (RoHS) aim to ban heavy metals such as lead. This pushes manufacturers to find functional and sustainable solutions with other solder alloys [2]. Consequently, a significant attention has been paid to the development of lead-free alloys. Among them, tin based alloys containing silver and copper (Sn-Ag-Cu) named SAC appear as the best alternative [7–9]. They present a good wettability, welding ability and mechanical properties. Furthermore, SAC alloys have a longer thermal fatigue life than classical Sn-Pb alloys [10–12].

Lastly a new type of solder ball was proposed: Polymer Core Solder Ball (PCSB). These are multi-material balls composed of a polymer core covered with different metallic coatings. Two types of PCSB can be found, those with a hard polymer core and with a soft polystyrene core. Figure 1-b and 1-c show soft PCSB, with copper, nickel-phosphorus and gold coatings that are used in this paper. These are made by electroless plating process. The PCSB are soldered with SAC solder paste to the component (SMD) and to the circuit board (PCB) to make the interconnection (see Figure 1-b). This system improves the mechanical robustness of the structure without compromising the electrical properties [13–15]. The plastic core relieves mechanical and thermal stresses in the solder joint enhancing reliability [16]. Several researchers have applied thermal fatigue test to BGA interconnections with PCSB and classical SAC solder balls [6, 10, 14, 17–20]. In all cases, the number of cycles to failure was greater with PCSB.

The use of these solder balls is very promising. However, literature remains limited regarding the characterization of the solder paste [19, 21–23] and in particular the interfaces between PCSB and SAC paste. These interfaces are considered as the weakest areas since an intermetallic layer (IMC) is created there during reflow [18, 19, 24].

Concerning the stiffness of the PCSB, it can be improved by: using hollow spheres [25], optimizing the thickness of the coatings and combining different coating materials [26–28]. Moreover, the choice of the coating materials is primordial to limit the IMC layer thickness and obtain more robust interconnections [24].

As observed, some research works analysed the influence of different parameters on the interconnection reliability . However, none analysed the interactions between them. The problem need to be studied more globally with numerical approaches. Multiple investigations dealt with the development of numerical models to predict solder ball behaviour under different mechanical [27, 29–34] and thermomechanical

[4, 20, 22, 33] conditions. All of them considered the mechanical properties of bulk materials to describe thin coatings. For instance, Young modulus (E) of bulk Nickel-Phosphorus was between 60-200 GPa [29–32] depending on the phosphorus content. For copper, Young modulus (E) was usually chosen between 110-130 GPa [31, 32, 34, 35] depending on crystal orientation.

It is known that the mechanical properties of coatings may differ from those of bulk material [30, 36]. Electroless plated materials show very fine micro crystalline and amorphous structures. This has an effect in the properties as smaller grain sizes lead to improvements in strength [37]. In electroless nickel-phosphorus plating, if phosphorus content is high the resulting coating is amorphous. This kind of materials are considered as metallic glasses, which are strong but brittle [38].

Mallory et al. [39] reported a Young modulus about 60 GPa and a tensile strength in the range 0.8-1.1 GPa for an amorphous Nickel-phosphorus coating. Electroless copper deposits in nonconductor substrates exhibit very fine and equiaxial grains [39]. Pauvonic [40] stated that tensile strenght of the copper coating could vary between 206-551 MPa depending on the grain size. These values are very different from bulk material. There is a clear need to mechanically characterize the properties of the coatings in order to build accurate numerical models.

This paper focuses on the micromechanical characterisation and the verification of electroless nickel-phosphorus and copper coatings mechanical properties using both experimental and numerical approaches. Nanoindentation and micropillar compression tests are conducted to quantify the elastic and plastic properties of the PCSB materials. A specific compression test at the PCSB scale is designed and performed to evidence occurrence of PCSB plastic flow. A finite element analysis of this compression test is conducted and the experimental results are compared to the experimental data. The first part of the paper deals with the description of the materials, sample preparation and characterisation methods. The second part is dedicated to materials characterization results. The last part details the PCSB compression test and discusses the importance of using mechanical properties measured at the right scale instead of using bulk-based mechanical properties.

2 Materials and methods

2.1 Polymer core solder balls (PCSB)

Polymer Core Solder Balls (PCSB) of 500 μm are produced from multi electroless plating processes (Figure 1-c) by HEF Groupe. They are composed by a polystyrene core coated with copper, nickel-phosphorus and gold as shown in Figure 1-d. The copper coating is 17 µm thick to provide a good electrical conductivity. The nickel-phosphorus coating of 5 µm stiffens the structure of PCSB and protects

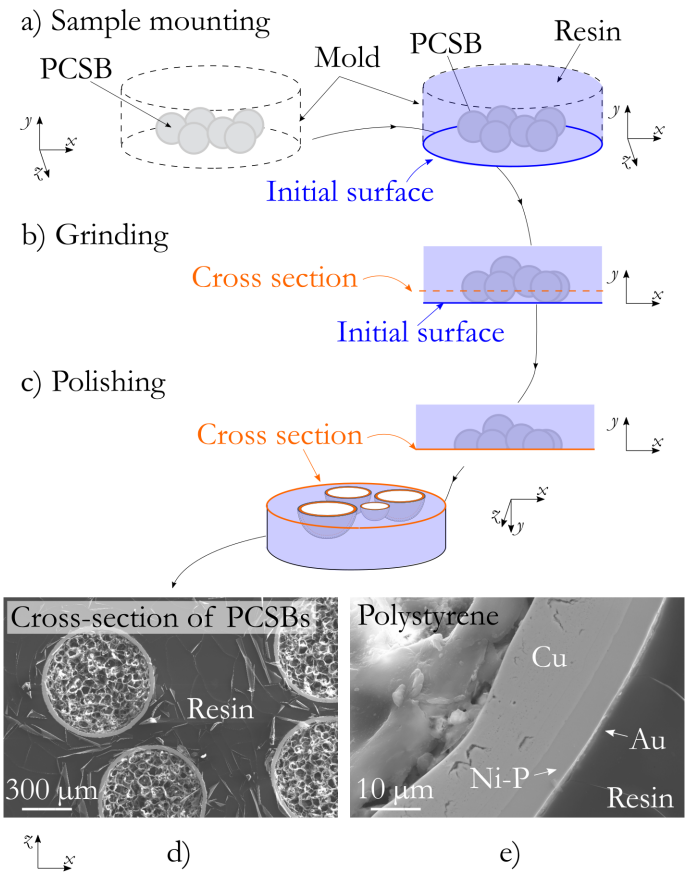

Figure 2: Sample preparation procedure: a) PCSB mounting in resin, b) Grinding until reaching the desired cross section, c) Mirror polishing of the sample, d) SEM image of the top view of the sample (cross-sectioned PCSBs) and e) a zoomed SEM image showing the polystyrene core, the copper layer (17 µm), the nickel phosphorus layer (6µm) and the gold coating of 70 nm.

copper from corrosion. Finally, a gold nano-coating of 70 nm is deposited to also protect the PCSB from corrosion during storage.

2.2 Sample preparation

Two samples with cross-sectioned PCSBs were meticulously prepared, procedure is shown in Figure 2. First, the PCSB solder balls were embedded in a non-conductive resin with a very low-shrinkage (EpoThin^{TM}, Buehler) (Figure 2-a)). Then, the samples were manually polished using SiC grit paper of P600 until reaching the desired solder ball cross-section (Figure 2-b)). Afterwards, the polishing with fabric and diamond suspension of 3 and 1 µm was carried out. Finally, samples were mirror polished by using a vibrometer (Buehler Vibropolish) with a colloidal silica suspension of 0.05 µm (MasterPolish^{TM}) diluted in water (50 %) during 4 hours (Figure 2-c). Figure 2-d shows a SEM image of the final surface that reveals the cross section of the PCSB solder balls. At higher magnification, the SEM image in Figure 2-e shows in detail the different layers of the PCSB: the copper layer with a thickness of 17 µm, the nickel phosphorus layer of 6 µm and the final gold coating of 70 nm.

In order to investigate the local mechanical properties of both coatings micromechanical tests were

performed on a mirror polished surface of cross-sectioned PCSBs. The nano-indentation tests determined the Young's modulus, while the micropillar compression tests provided the yielding limits of Cu and Ni-P coatings. The testing procedures are precised in sections 2.4 and 2.3.

2.3 Nano-indentation tests

Nanoindentation grids were performed in the cross section of the PCSB coating layers as Figure 3-a and 3-b show. A defect-free region of the sample has been deliberately selected for conducting the nano indentation tests. A Nano Indenter XP ®system (DCM of MTS Nano Instruments) was used with an Berkovich diamond tip. A normal load is applied to the tip to indent the material, while both the load and the displacement are tracked (see Figure 3-c). The penetration depth was set to 300 nm and the indents were spaced about 3 µm. This test permit to measure the hardness H and the elastic modulus E of a material [41]. Only the elastic modulus will be estimated by nano-indentation tests. The plastic flow properties will be measured by micropillar compression tests (see section 2.4). To that aim, the slope S of the unloading part of the curve is considered, which corresponds to the elastic stiffness of the contact (see Figure 3-c). Equations 1 and 2 are applied to obtain the elastic modulus E, where $E_c'^*$ is the contact elastic modulus, A_c the projected contact area, $E_i'^*$ the reduced elastic modulus of the indenter and $\nu_i'^*$ and ν'^* are the Poisson ratio of the indenter and the sample [42]. The projected contact area is computed using the Oliver and Pharr's model [43].

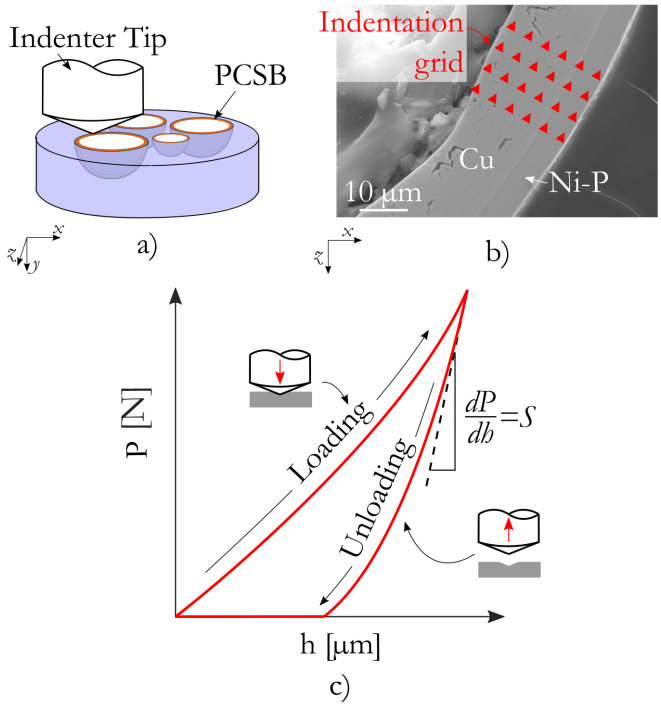

Figure 3: Nanoindentation procedure: a) Illustration of the position of the sample concerning the indenter, b) the position of the indentation grid in the PCSB coating layers and c) the typical load-displacement curve obtained during the test.

$$E_c'^{*} = \frac{S}{2}\sqrt{\frac{\pi}{A_c}} \tag{1}$$

$$\frac{1-\nu^2}{E} = \frac{1}{E_c'^{*}} - \frac{1-\nu_i^2}{E_i'^{*}} \tag{2}$$

2.4 Micro pillar compression tests

For each coating (copper and nickel-phosphorus), three micro pillars were machined in the previously cross sectioned and polished PCSB sample. The illustrations in Figure 4-a show the sample, the cross-sectioned PCSB and the orientation and position of the micro pillars concerning the coating layers. Figure 4-b and 4-c show the SEM images of the PCSB and the micro pillars.

The machining of the pillars was carried out with a Thermo Scientific Helios NanoLab DualBeam 600i FIB/SEM. The geometry of the pillars was obtained first applying high currents (30 kV, 2.5 A). Then the final shape is achieved with a gradual decrease of the current until 80 pA. Copper pillars had a diameter $\varnothing$ of 3 µm and they were 6 µm high (h_{pil0}), whereas nickel pillars had a diameter $\varnothing$ of 2 µm and a height (h_{pil0}) of 4 µm. The nickel pillars were smaller due to the small thickness of the nickel coating.

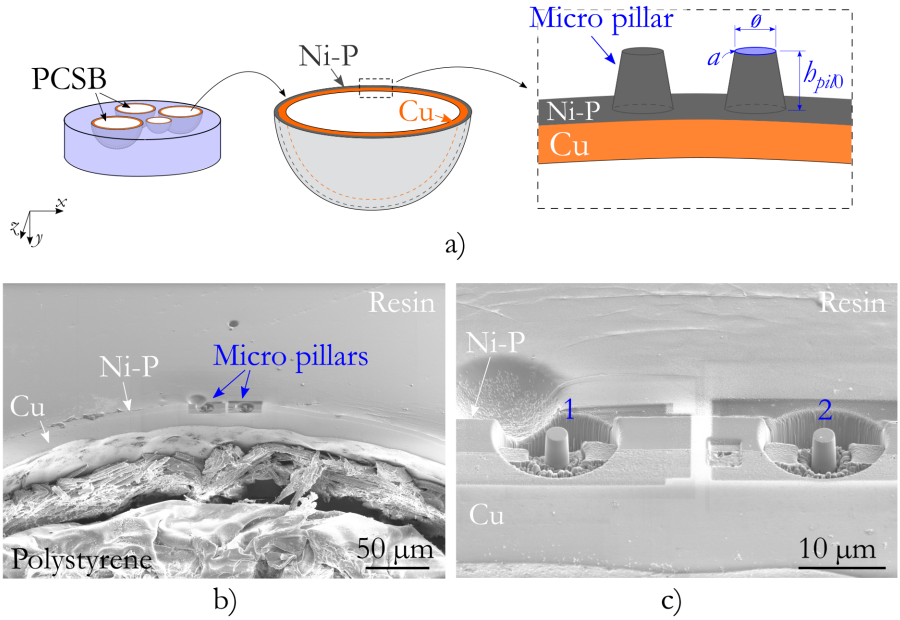

Figure 4: a) Illustration of the position and the orientation of micro pillars concerning the coatings of PCSB, b) and c) SEM images of the micro pillars in the nickel phosphorus coating.

For insitu micropillar compression tests, an ALEMNIS nanoindenter was employed. The system was installed in a Zeiss Gemini supra 55VP Scanning Electron Microscope (SEM) as shown in Figure 5-a. The sample is placed above the load cell and under a diamond flat-punch (ALS/FLT060/D005) with a

diameter of 5 µm. The test consists in compressing the pillar with the punch while tracking the local load-displacement curve (see Figure 5-b). The applied displacement to the punch varied between the materials due to differences in pillar dimensions. The applied displacement for copper pillars was 4 µm, while for nickel-phosphorus pillars, it was 3 µm. SEM micrographs on Figures 5-c and d show the pillars before and after compression. The displacement curve was corrected taking into account a stiffness k that accounts for the frame system (1100 mN/µm), compared to this value the substrate stiffness was considered negligible [44]. The equation 3 was used where u_{real} is the true vertical deformation applied to the pillar, u_{mes} the measured punch displacement and F the measured load:

$$u_{real} = u_{mes} - F/k \tag{3}$$

Then, the load-displacement curve was converted to true stress-true strain following the methodology proposed in [45], based on equations 4 and 5, where ε is the true strain, σ the true stress, h_{pil_0} is the initial height of the pillar, h the pillar height and A the pillar section ($A = \pi a^2$) at time t. From the true stress-strain curve, the yield strength value was retained.

$$\varepsilon = ln(h/h_{pil_0}) \tag{4}$$

$$\sigma = F/A \tag{5}$$

3 Mechanical properties of Cu and Ni-P coatings

3.1 Results of the micromechanical tests

The yielding strength (σ_y) and the Young modulus (E) of copper and nickel-phosphorus coatings were characterized by means of micro pillar compression and nanohardness tests. Table 1 resumes the values for both materials and compares characterised values with those from literature. Figure 6 shows the true stress-strain curves obtained by microcompression testing on copper and nickel-phosphorus pillars. For each material, three pillars were tested and the results are plotted in orange and in blue for Cu and Ni-P. All Cu pillar tests are repeatable, whereas $Ni-P$ curves presented a slightly different behaviour in the plastic region. However, the curves were considered valid as only the yielding limit σ_y is retained. The values for the coating of copper ($\sigma_{y_{Cu}}$) and nickel-phosphorus ($\sigma_{y_{Ni-P}}$) are 0.6 GPa and 1.7 GPa. These are consistent with electroless plating copper and nickel-phosphorus yielding limits that Mallory et

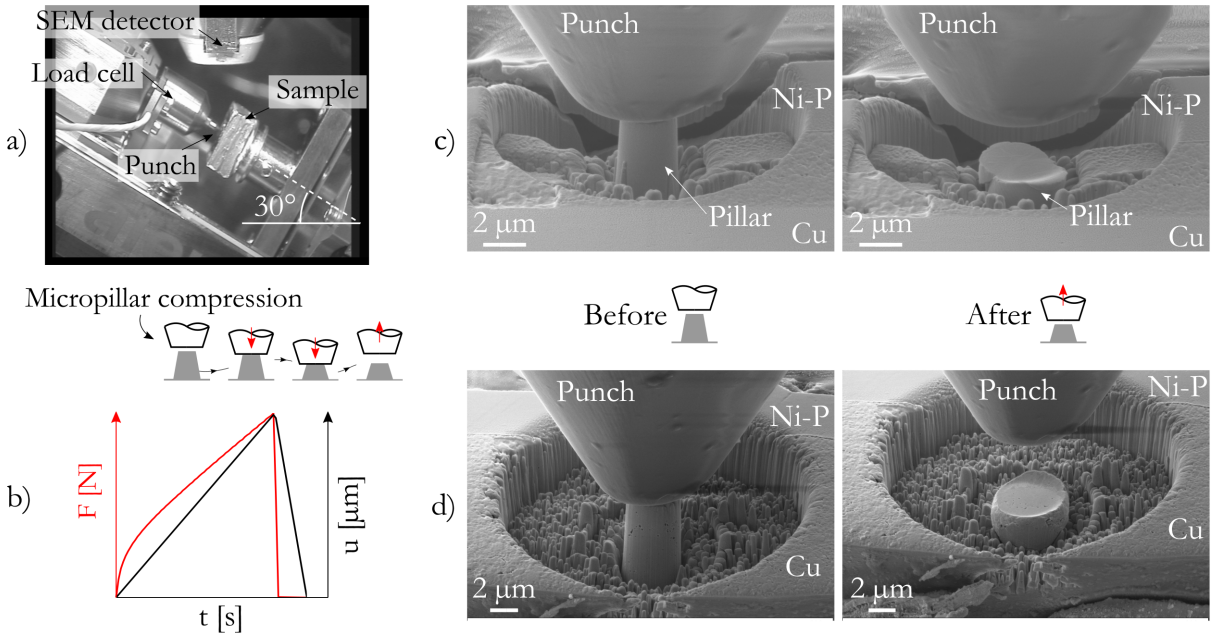

Figure 5: a) Alemnis nanoindenter system inside the SEM with a orientation of 30°, b) an schematic description of the micropillar compression tests and the typical load-time and load displacement curves, c) SEM micrographs of nickel-phosphorus micro pillar and d) copper micro pillar before and after compression.

al. and Pauvonic [39,40] presented. Nevertheless, these values significantly deviate from bulk properties. It can be observed that both materials rapidly reach a stress plateau, indicating a near-perfectly plastic flow and absence of hardening. This is expected for amorphous materials [45] and for nanocrystalline materials [46].

Concerning the young modulus (E), the measured values by nanohardness tests are 100 GPa and 110 GPa for copper and nickel phosphorus. These are lower than bulk material values. In the case of Cu, the discrepancy with a bulk material is slight and can be explained by the remaining presence of some defects between Cu layers. In the case of Ni-P, this is likely a consequence of the phosphorus content that can play on the microstructure. For instance, Sanderson [47] wrote that a nominal 10.5% P lead to Young modulus close to 115 GPa due to the amorphous nature of the material. In the present investigation the nominal content was estimated to be close to 8% P.

Indeed, it is well known that the nature of the microstructure of the materials defines their mechanical behaviour. With the aim of understanding the difference observed between electroless plated and bulk materials, microstructure of the coatings is characterised in more detail in the following section.

Material	Source	Young modulus (E) [GPa]	Yield stress (σ_y) [MPa]
Cu	Micromechanics Bibliography	100 130 [31,32,34,35]	600 30 [48]
Ni	Micromechanics Bibliography	110 60-200 [29–32]	1700 500-1000 [39]

Table 1: Material properties of Cu and Ni-P coatings obtained from micromechanical characterisation and from bibliography.

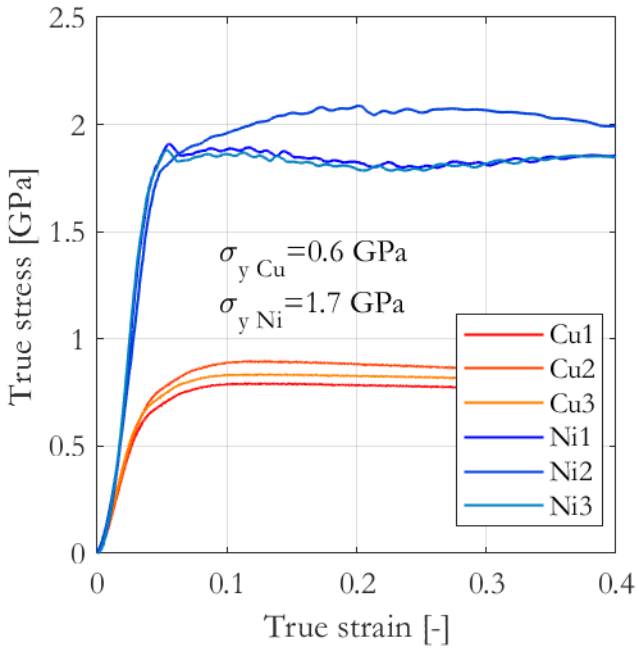

Figure 6: True stress-true strain curves for copper pillars (Cu 1-3) and nickel-phosphorus (Ni 1-3) pillars.

3.2 Correlation with the microstructure

Previous observations of the cross-sectioned PSCB in SEM did not reveal the nanostructure of the coatings. In order to identify in more detail the microstructure of those thin films, a thin lamella was extracted from a PCBS using a Focus Ion Beam (FIB) as shown in Figure 7-a. This foil was then mounted on a specific sample holder, allowing to observe it in transmission directly in the SEM. Figure 7-b shows the microstructure of the coatings observed in STEM mode. The nickel-phosphorus coating shows a uniform contrast. In the contrary, in the copper coating, a nanocrystalline structure can be distinguished. In order to obtain more information of the grain size, morphology, distribution and crystallographic orientations, a TKD analysis is performed using an Oxford Symmetry II camera. Figure 7-b shows the superimposed band-contrast and Euler-angles maps of the two coatings: the upper black area corresponding to the nickel-phosphorus coating and the middle coloured section corresponding to the copper coating.

The non-indexation of the region comprising the Ni-P coating is likely a consequence of its amorphous nature. This was expected as the coating has a high phosphorus content (8% by weight) [38]. Concerning the Cu coating, despite their extreme fineness, some grains were revealed. It can be said that the size of the grains varies between 20 and 100 nm, and that their shape seems mainly equi-axial even if some of them present a columnar shape. In areas where the indexation is low, it is assumed that the grain size is less than 20 nm. Finally, no preferential crystallographic orientation is observed.

These observations confirm that the microstructure of the two coatings differs from that of the raw

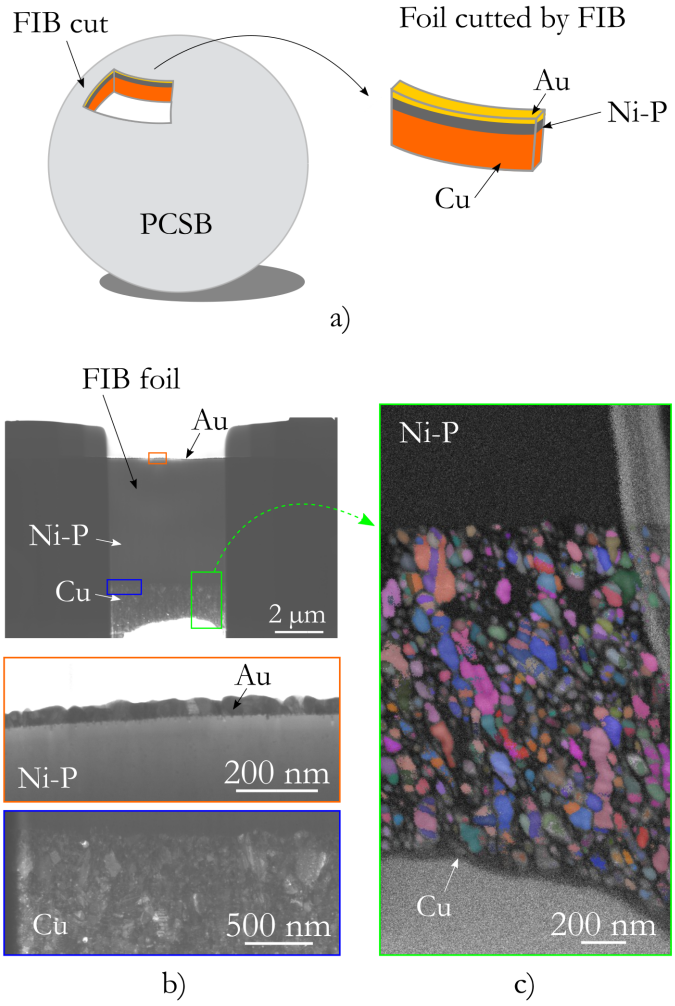

Figure 7: a)Illustration of the PCSB and the foil, b) SEM images of the foil and detail of the copper, nickel-phosphorus and gold coating microstructures and c) the band contrast image with the Euler angles from TKD analysis.

material, with the consequence that their mechanical behaviour is different. Amorphous Ni-P is considered to be a metallic glass [38], and are known to be hard but brittle materials. This explains the measured high yield strength and low Young's modulus.

In general, the smaller the grain size, the higher the strength of the material [37]. This is precisely what we have observed for Cu, which with its nano-crystalline structure has a really high yield strength. More specifically the measured yield stress (0.6 GPa) is very consistent with the results of Dao et al [46] on nanocrystalline Cu. According to their paper it corresponds to an average grain size of 50 nm.

This section has revealed the huge differences between raw materials and electroless plated coatings. We therefore draw attention to the use of raw material properties to describe the behaviour of thin coatings in numerical models, which is very common in the literature, but which can lead to inaccurate or even incorrect analysis.

4 Validation of the mechanical properties at the PCSB scale

The validation of the characterised material properties is conducted thanks to a mesoscopical scale study. To that aim, the behaviour of PCSB solder balls under compression is analysed. Both numerical and experimental approaches are combined. Figure 8-a shows the employed sample: PCSB solder balls are brazed to the circuit board with a SAC 305 welding paste. The PCSB are compressed by a flat indenter (Figure 8-b) and the resulting load (F) is tracked and plotted against the displacement of the indenter as shown in Figure 8-c.

First, the numerical model is built and two calculations are done, one with the previously characterised material properties and the other with the properties obtained from literature. Then, the results are compared to the experimental ones. Finally, the correlation of experimental and numerical results allows the identification of most appropriate material properties.

4.1 Description of the numerical model

The geometrical parameters of both the solder ball (PCSB) and the solder joint are obtained from the sample used in the experimental tests (see Figure 8). The PCSB is modeled as a hollow sphere since the core material, a porous polymer, does not contribute to the mechanical functionality of the solder ball. The configuration can be simplified in a 2D axisymmetric model. The commercial code Abaqus/Standard was used.

The model was divided in two parts (Figure 9-a). Together the PCSB and the solder joint made up the first axisymmetric Lagrangian deformable part. Figure 9-b shows three sections corresponding to

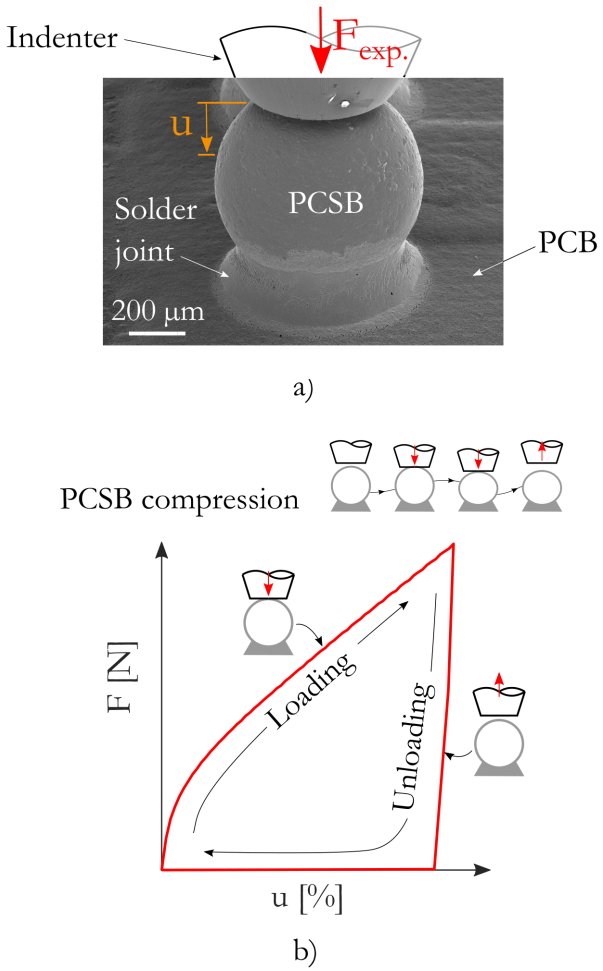

Figure 8: PCSB compression tests: a) the position of the indenter and the PCSB and b) the resultant load vs. displacement curve.

three materials: copper, nickel-phosphorus and the solder paste SAC305. The dimensions were r_1=355 µm, r_2=333 µm, h_1=10 µm, h_2=200 µm, e_{Cu}=17 µm, e_{Ni-P}=5 µm. The bottom surface of the solder joint was constrained in x and y directions as indicated in Figure 9-b. The second part represents the indenter, it is considered as an axisymmetric discrete rigid plate. Movements are allowed in the vertical direction y.

The deformable part was meshed with 4 node bilinear (called CAX4R) and 3 node linear elements (CAX3). The 4 node elements were used to mesh the PCSB section with a uniform distribution, whereas the 3 node elements to mesh the solder joint with a non uniform distribution. The approximate size of the elements was 1.1 µm. The contact interation between the punch and the PCSB external surface is defined by a kinematic contact algorithm with a finite sliding formulation.

Three materials are defined in the model: copper, nickel-phosphorus and SAC305. In this study, two different copper and nickel-phosphorus materials are compared: the first simulation considers the properties found in literature [29–32] and the second one the properties characterized by the micromechanical tests presented in section 3. The material properties of SAC305 were found in [31]. Table 2 reports the

employed parameters in both simulations.

The indenter deforms the PCSB inducing stresses through all the structure (PCSB and solder joint). In this study, the reaction force ($F_{num.}$) on the center of the indenter is tracked and plotted against the displacement (u) as shown in the illustration in Figure 8-c. This curve permits to analyse the behaviour of the solder ball under compression for both types of materials.

Figure 10-b in section 4.3 show the numerical force against the displacement of the punch extracted from both simulations.

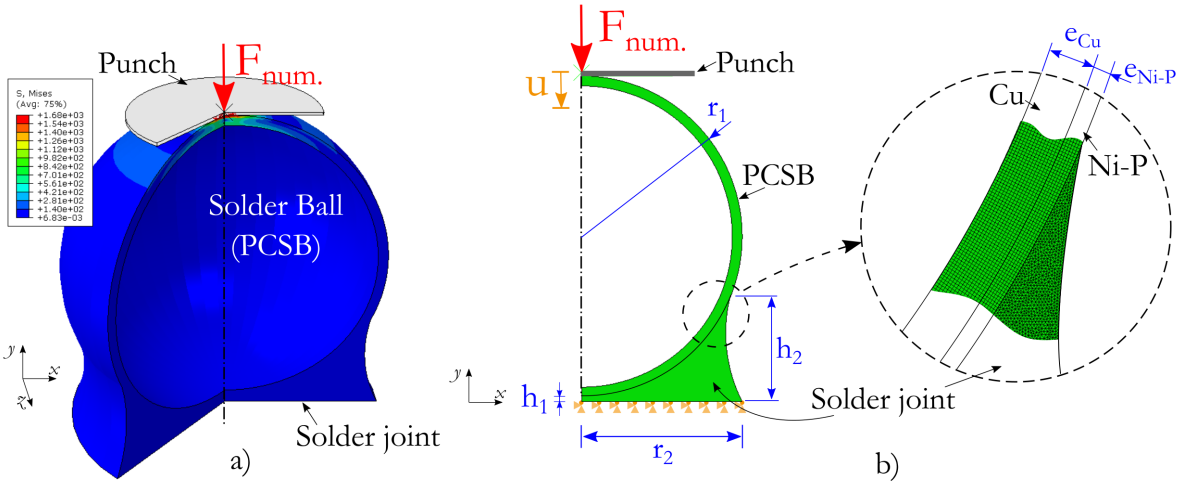

Figure 9: a) The model with the solder ball and the punch during compression and b) the sections, dimensions, the mesh, boundary conditions and the output parameter (F_{num}) of the model.

Simulation reference	Cu			Ni-P			SAC305		
	E [GPa]	σ_y [MPa]	ν [-]	E	σ_y	ν	E	σ_y	ν
Num. Bibliography	130	33	0.34	210	480	0.31	50	20	0.34
Num. Micro mechanics	80	600	0.34	120	1700	0.31			

Table 2: Material properties of Cu and Ni-P coatings and SAC305 solder paste used in two simulations.

4.2 Experimental PCSB compression tests

The sample shown in Figure 8-a was placed in the ALEMNIS in-situ nanoindenter system presented in section 2.4. However, the employed indenter was replaced by a larger one with a diameter of 500 µm and a load cell with a stiffness k of 250 mN/µm was used instead. The system was placed in the SEM and the indenter was placed above the PCSB ball (Figure 8-a). Then, the indenter was displaced by 10 µm to compress the PCSB. The reaction force (F) was tracked during the loading-unloading process. The displacement curve was corrected as in section 2.4, the real compression distance applied to the PCSB was 4 µm. The test was repeated five times in different PCSB to ensure the repeatability of the experiment. The five curves are plotted in Figure 10-a in section 4.3.

4.3 Results

Figure 10 plots the reaction force (F) againts the applied displacement (u) during the PCSB compression tests for both numerical and experimental approaches. The data series for the numerical curves are plotted in black with dotted lines in Figure 10-b, whereas those for the experimental curves are plotted in Figure 10-a in green and blue with solid lines. The experimental curves show a good repeatability of the experiments even if the maximum force $F_{max.}$ varied of $\pm$ 0.08 N from an experiment to another. The mean value for the maximum force was of 0.96 N. An hysterisis is observed on each curve. It is likely the signature of plastic flow occurring in Cu or Ni-P coatings. Concerning the numerical results, both curves show a different mechanical behaviour of the PCSB. The maximal force $F_{max.}$ for the bibliography data simulation was of 0.25 N, whereas 0.94 N for the micro-mechanics data simulation. The experimental curve matches quite well with the numerical curve when mechanical properties used in the FEM are those measured from micromechanical tests. In Figure 10-b, the error in the maximum force is about 2.1 %. On the contrary the numerical curve resulting from literature-based mechanical properties significantly differs from experimental curves. It can be easily explained by the lower yield stress of bulk Cu, which lead to a premature yielding and thus to significant hysterisis after unloading. This validates the mechanical properties measured from the micromechanical tests presented in this paper as well as the proposed PCSB compression numerical model.

These results highlight the interest of a methodology based on micromechanical tests to measure mechanical properties of PCSBs in view of using them in finite element analyses. More specifically it points out the importance of using the real mechanical properties to predict PCSBs sustainibility during the design stage. For instance, using literature data would have led to increase Cu and/or Ni-P thicknesses and thus to additional costs and weight. In this paper, only Room Temperature mechanical properties are investigated whereas PCSBs should sustain load at varying temperature that can be down to -50°c and up to 150°C. Thanks to intense developments in micromechanical testing in the past decade, high and low temperature micropillar compression are now available [49, 50]. Also cyclic/fatigue behaviour at the micronscale can be investigated thanks to high frequency micromechanical tests [51]. In the upcoming years, it is likely that these new capacities in micromechanical testing may help the design micro-electronic components such as PCSBs by loading materials at the right temperature, at the right scale with the right frequency.

5 Conclusion

The objective of this work was to investigate material properties of metal coatings commonly used in the field of electronic packaging. For the first time, a PCSB (Polymer Core Solder Ball) coatings

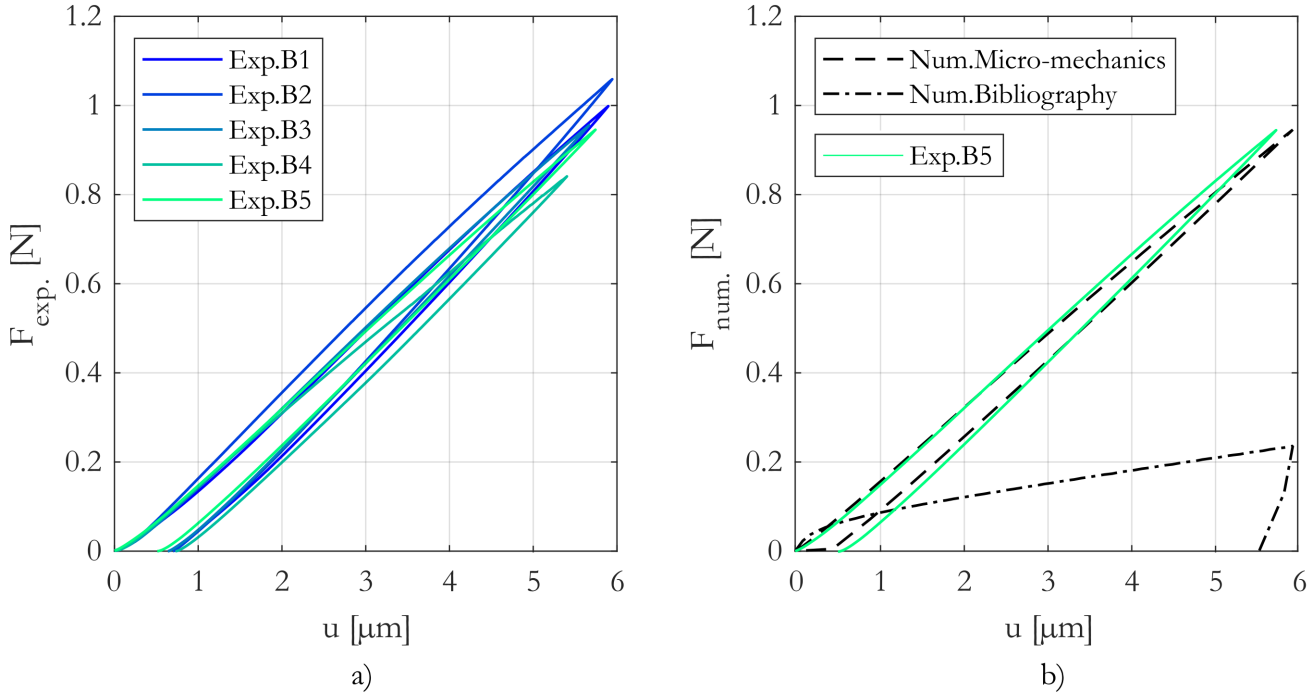

Figure 10: Force-displacement curves resulting of PCSB compression. Left - experimental data, right - comparison with numerical results. PCSB compression results are well reproduced when mechanical properties used in the FEM are those measured from micromechanical tests.

were characterized by insitu micropillar compression and nanohardness tests. Then a macroscale study permitted to verify the parameters. The main conclusions can be drawn as follows:

- The yielding strength of electroless plated copper and nickel coatings were 0.6 GPa and 1.7 GPa respectively. Regarding the Young modulus, their respective values are 100 GPa and 120 GPa.
- Electroless plated copper resulted in a nanocrystalline material, grains size varied between 20 and 100 nm. The electroless plated nickel-phosphorus (8% by weight) was amorphous.
- The PCSB behaviour under compression was studied with the characterized material properties. The numerical results are consistent with experimental ones.
- This paper highlights the interest of a methodology based on micromechanical tests to measure mechanical properties of materials in electronics.

The present work enabled the acquisition of the local mechanical properties of the Cu and Ni-P coatings. A future research direction will involve analyzing the thermal fatigue behaviour of PCSB solder balls. To accomplish this, test vehicles will be fabricated using both PCSB and SAC solder balls and subjected to rapid temperature variation tests. Subsequently, the test vehicles will be cross-sectioned to observe the damage modes and gain a deeper understanding of the failure mechanisms associated with both PCSB and SAC solder balls.

Acknowledgements

The authors would like to thank La Region for the financial funding of the project SuperBall. S.Girard-Insardi and M. Mondon are thanked for the technical support.

References

[1] Gheorghe Pascariu, Peter Cronin, and Daniel Crowley Mrsi. Next generation electronics packaging utilizing flip chip technology. *2003 IEEE/CPMT/ISEMI lnT Electronics Manufacturing Technolcgy Sympsium*, 2003.

[2] King-Ning Tu. *Solder Joint Technology: Materials, Properties and Reliability*, volume 92. Springer New York, NY, 2007.

[3] Olivier Gaillard. Board level reliability testing of hermetic packages equipped with high-rel interconnection solutions and dedicated to space applications. In *2013 Eurpoean Microelectronics Packaging Conference (EMPC)*, pages 1–8, 2013.

[4] Joshua A. Depiver, Sabuj Mallik, and Emeka H. Amalu. Thermal fatigue life of ball grid array (bga) solder joints made from different alloy compositions. *Engineering Failure Analysis*, 125:105447, 7 2021.

[5] Darrel R. Frear, Steven N. Burchett, Harold S. Morgan, and John H. Lau. *Mechanics of Solder Alloy Interconnects*. Springer New York NY, 1994.

[6] Hiroya Ishida and Kiyoto Matsushita. Characteristics of ceramic bga using polymer core solder balls. *Proceedings - Electronic Components and Technology Conference*, pages 404–410, 9 2014.

[7] Schmetterer C., Ipser J., and Pearce. Handbook of properties of sac solders and joints: Elfnet/cost 531 lead free solders database, 2008.

[8] Hiren R. Kotadia, Philip D. Howes, and Samjid H. Mannan. A review: On the development of low melting temperature pb-free solders. *Microelectronics Reliability*, 54:1253–1273, 6 2014.

[9] Xiaoyan Niu, Guoqiang Dong, Xiaomeng Li, Xuchen Geng, and Jiang Zhou. Effect of indentation depth and strain rate on mechanical properties of sn0.3ag0.7cu. *Microelectronics Reliability*, 128:114429, 1 2022.

[10] T. Kangasvieri, O. Nousiainen, J. Putaala, R. Rautioaho, and J. Vähäkangas. Reliability and rf performance of bga solder joints with plastic-core solder balls in ltcc/pwb assemblies. *Microelectronics Reliability*, 46:1335–1347, 8 2006.

[11] Bo Liu, Tae Kyu Lee, and Kuo Chuan Liu. Impact of 5reliability of wafer-level packages with sn-pb and sn-ag-cu solder interconnects. *Journal of Electronic Materials*, 40:2111–2118, 10 2011.

[12] Maurice N. Collins, Jeff Punch, Richard Coyle, Michael Reid, Richard Popowich, Peter Read, and Debra Fleming. Thermal fatigue and failure analysis of snagcu solder alloys with minor pb additions. *IEEE Transactions on Components, Packaging and Manufacturing Technology*, 1:1594–1600, 10 2011.

[13] Jani Miettinen, Jarmo Tanskanen, and Eero O. Ristolainen. Stacked 3-d mcp with plastic ball vertical interconnections. *Proceedings - Electronic Components and Technology Conference*, pages 1101–1105, 2003.

[14] Sashidhar Movva and Gerardo Aguirre. High reliability second level interconnects using polymer core bgas. *Proceedings - Electronic Components and Technology Conference*, 2:1443–1448, 2004.

[15] Karthik Thambidurai, Viren Khandekar, Tiao Zhou, and Kaysar Rahim. Development of low cost and high pin count wafer level packaging. pages 66–71, 2015.

[16] Karl J. Puttlitz, Thomas Caulfield, and Marie Cole. Effect of material properties on the fatigue life of dual solder (ds) ceramic ball grid array (cbga) solder joints. *Proceedings - Electronic Components and Technology Conference*, pages 1005–1010, 1995.

[17] N. Okinaga, H. Kuroda, and Y. Nagai. Excellent reliability of solder ball made of a compliant plastic core. *Proceedings - Electronic Components and Technology Conference*, pages 1345–1349, 2001.

[18] Jesse Galloway, Ahmer Syed, Won Joon Kang, Jin Young Kim, Jeff Cannis, Yun Hyeon Ka, Seung Mo Kim, Tae Seong Kim, Gi Song Lee, and Sang Hyun Ryu. Mechanical, thermal, and electrical analysis of a compliant interconnect. *IEEE Transactions on Components and Packaging Technologies*, 28:297–302, 6 2005.

[19] Yeng Ping Wang, Liang Yi Hung, Don Son Jiang, Chiang Cheng Chang, Yu Po Wang, and C. S. Hsiao. High drop performance interconnection: Polymer cored solder ball. *Proceedings - Electronic Components and Technology Conference*, pages 1208–1211, 2008.

[20] X. J. Fan, B. Varia, and Q. Han. Design and optimization of thermo-mechanical reliability in wafer level packaging. *Microelectronics Reliability*, 50:536–546, 4 2010.

[21] J. Y. Son, S. G. Lee, Y. W. Lee, and S. B. Jung. Mechanical property and plated solder volume effect of cu core ball. *2018 IEEE 20th Electronics Packaging Technology Conference, EPTC 2018*, pages 137–142, 12 2018.

[22] Solder joint reliability investigation of chip scale package with plastic core solder balls on thermomechanically loaded pcbs. *Proceedings - Electronic Components and Technology Conference*, 2016-August:244–250, 8 2016.

[23] Seppo K. Pienimaa, Jani Miettinen, and Eero Ristolainen. Stacked modular package. *IEEE Transactions on Advanced Packaging*, 27:461–466, 8 2004.

[24] M.M.V. Taklo, J. Seland Graff, D. Nilsen Wright, H. Kristiansen, L. Hoff, and K. Waaler. Failure analysis of thermally and mechanically stressed plastic core solder balls. IEEE, 2013.

[25] Thomas F. Marinis and Joseph W. Soucy. Design of bga assemblies with enhanced thermal cycle capability using solder coated polymer balls. *International Symposium on Microelectronics*, 2016:000123–000133, 10 2016.

[26] Yap Boon Kar, Tan Cai Hui, Ramasamy Agileswari, and Calvin Lo. Comparison study on reliability performance for polymer core solder balls under multiple reflow and hts stress tests. *Microelectronics Reliability*, 53:164–173, 1 2013.

[27] Yap Boon Kar, Tan Cai Hui, Agileswari, and Calvin Lo. Solder ball robustness study on polymer core solder balls for bga packages. *Proceedings of the IEEE/CPMT International Electronics Manufacturing Technology (IEMT) Symposium*, 2012.

[28] Hiroya Ishida. Reliability innovation in large size fine pitch wlcsp, 2012.

[29] Bin Xie, X. Q. Shi, and Han Ding. Investigation of mechanical and electrical characteristics for cracked conductive particle in anisotropic conductive adhesive (aca) assembly. *IEEE Transactions on Components and Packaging Technologies*, 31:361–369, 2008.

[30] Molly Bazilchuk, Takashi Sumigawa, Takayuki Kitamura, Zhiliang Zhang, Helge Kristiansen, and Jianying He. Contact area measurement of micron-sized metal-coated polymer particles under compression. *International Journal of Mechanical Sciences*, 165, 1 2020.

[31] K. Weide-Zaage, J. Schlobohm, R. T.H. Rongen, F. C. Voogt, and R. Roucou. Simulation and measurement of the flip chip solder bumps with a cu-plated plastic core. *Microelectronics Reliability*, 54:1206–1211, 6 2014.

[32] Jong Woong Kim and Seung Boo Jung. Experimental and finite element analysis of the shear speed effects on the sn–ag and sn–ag–cu bga solder joints. *Materials Science and Engineering: A*, 371:267–276, 4 2004.

[33] Huai Hui Ren, Xi Shu Wang, and Su Jia. Fracture analysis on die attach adhesives for stacked packages based on in-situ testing and cohesive zone model. *Microelectronics Reliability*, 53:1021–1028, 7 2013.

[34] Xi Shu Wang, Su Jia, Huai Hui Ren, and Pan Pan. Effects of solder balls and arrays on the failure behavior in package-on-package structure. *Microelectronics Reliability*, 54:633–640, 3 2014.

[35] Yeong K. Kim, Jin Hyuk Gang, and Bo Young Lee. Material property effects on solder failure analyses. *Microelectronics Reliability*, 51:985–993, 5 2011.

[36] Molly Bazilchuk, Otto Magnus Evenstad, Zhiliang Zhang, Helge Kristiansen, and Jianying He. Resistance analysis of spherical metal thin films combining van der pauw and electromechanical nanoindentation methods. *Journal of Electronic Materials*, 47:6378–6382, 11 2018.

[37] Zbigniew H Stachurski, Gang Wang, and Xiaohua Tan. Chapter 1 - introduction, 2021.

[38] R N Duncan. The metallurgical structure of electroless nickel deposits:effect on coating properties, 1996.

[39] Glenn 0 Mallory and Juan B Hajdu. Electroless plating : Fundamentals and applications, 1990.

[40] Milan Paunovic. Electroless deposition of copper, 2010.

[41] Anthony C. Fischer-Cripps. *Nanoindentation*. 2002.

[42] G. Guillonneau, G. Kermouche, S. Bec, and J. L. Loubet. A simple method to minimize displacement measurement uncertainties using dynamic nanoindentation testing. *Tribology International*, 70:190–198, 2 2014.

[43] Warren Carl Oliver and George Mathews Pharr. An improved technique for determining hardness and elastic modulus using load and displacement sensing indentation experiments. *Journal of materials research*, 7(6):1564–1583, 1992.

[44] Rémi Lacroix, Vincent Chomienne, Guillaume Kermouche, Jérémie Teisseire, Etienne Barthel, and Samuel Queste. Micropillar testing of amorphous silica. *International Journal of Applied Glass Science*, 3(1):36–43, 2012.

[45] G Kermouche, G Guillonneau, J Michler, J Teisseire, and E Barthel. Perfectly plastic flow in silica glass. *Acta Materialia*, 114:146–153, 2016.

[46] M Dao, L Lu, RJ Asaro, J Th M De Hosson, and E Ma. Toward a quantitative understanding of mechanical behavior of nanocrystalline metals. *Acta Materialia*, 55(12):4041–4065, 2007.

[47] Terry Sanderson. Measuring the elastic moduli of electroless nickel-phosphorus deposits. *Plating and surface finishing*, 92(6):39–43, 2005.

[48] Matweb.

[49] Ariane Viat, Gaylord Guillonneau, Siegfried Fouvry, Guillaume Kermouche, Sergio Sao Joao, Juri Wehrs, Johann Michler, and Jean-François Henne. Brittle to ductile transition of tribomaterial in relation to wear response at high temperatures. *Wear*, 392:60–68, 2017.

[50] Keith Thomas, Gaurav Mohanty, Juri Wehrs, Aidan A Taylor, Siddhartha Pathak, Daniele Casari, J Schwiedrzik, N Mara, Ralph Spolenak, and Johann Michler. Elevated and cryogenic temperature micropillar compression of magnesium–niobium multilayer films. *Journal of materials science*, 54:10884–10901, 2019.

[51] Sebastian Krauß, Thomas Schieß, Mathias Göken, and Benoit Merle. Revealing the local fatigue behavior of bimodal copper laminates by micropillar fatigue tests. *Materials Science and Engineering: A*, 788:139502, 2020.